frontiers
in Astronomy and
Space Sciences

TYPE Original Research
PUBLISHED 17 March 2026
DOI 10.3389/fspas.2026.1729075

OPEN ACCESS

EDITED BY
Anasuya Aruliah,
University College London,
United Kingdom

REVIEWED BY
Robin Wing,
Leibniz Institute of Atmospheric Physics (LG), Germany
Timothy Paul Banyard,
University of Bath, United Kingdom

*CORRESPONDENCE
Wenjun Dong,
dongw1@erau.edu

RECEIVED 20 October 2025
REVISED 26 January 2026
ACCEPTED 16 February 2026
PUBLISHED 17 March 2026

CITATION
Dong W, Liu AZ, Hoffmann L, Fritts DC, Yang F and Hu J (2026) Seasonal vertical coupling of gravity waves over the Southern Andes from 3D satellite and high-resolution lidar observations. *Front. Astron. Space Sci.* 13:1729075. doi: 10.3389/fspas.2026.1729075

Seasonal vertical coupling of gravity waves over the Southern Andes from 3D satellite and high-resolution lidar observations

Wenjun Dong[1,2]*, Alan Z. Liu[1], Lars Hoffmann[3], David C. Fritts[2], Fan Yang[1] and Jiahui Hu[1]

[1]Center for Space and Atmosphere Research, Embry-Riddle Aeronautical University, Daytona Beach, FL, United States, [2]Global Atmospheric Technologies and Sciences, Boulder, CO, United States, [3]Jülich Supercomputing Center, Forschungszentrum Jülich, Jülich, Nordrhein-Westfalen, Germany

In the mesosphere, vertical wind velocities can exceed tens of m/s, driven by gravity wave (GW) processes such as wave breaking and the generation of secondary GWs. These dynamic events play a crucial role in redistributing energy and momentum across atmospheric layers. In this study, we investigate the GW dynamics over the Southern Andes—a prominent hotspot for GW activity—using a combination of satellite and ground-based observations. In particular, we analyze nearly two decades of atmospheric infrared sounder (AIRS) data, along with approximately 5 years of sodium (Na) lidar observations from the Andes Lidar Observatory (ALO). Our analysis reveals a clear seasonal co-variation between lower-stratospheric GW activity and mesospheric perturbations, with both datasets exhibiting pronounced austral-winter enhancements. The mesospheric Na-lidar variance also exhibits secondary maxima during late summer and spring; a simple vertical-wavenumber spectral analysis indicates that these shoulder enhancements result from modest, broadband increases in short-vertical-wavelength power. This variability is consistent with vertical coupling mediated by seasonally varying background winds and mesospheric wave dissipation.

KEYWORDS
Andes, gravity wave, mesosphere, stratosphere, vertical coupling

1 Introduction

Gravity waves (GWs) are atmospheric disturbances that transport energy and momentum vertically and horizontally, thereby coupling different atmospheric layers (Fritts and Alexander, 2003; Alexander et al., 2008). They play a fundamental role in driving the general circulation of the middle atmosphere by carrying momentum from the troposphere into the stratosphere and mesosphere, where their dissipation induces mean-flow accelerations and modulates large-scale circulation patterns. Major sources of GWs include orography (mountain waves generated by airflow over topography), deep convection, frontal systems, volcanic eruption, seismic and anthropogenic explosions, and wind-shear instabilities (Fritts and Alexander, 2003; Sato et al., 2009; Dong et al., 2023; Dong et al., 2020; Fritts et al., 2020; Inchin et al., 2022; Chau et al., 2024). Among these, orographic (mountain-induced) GWs are particularly

important in well-known global hotspots, such as the Southern Andes and the Antarctic Peninsula, where strong winds impinging upon steep terrain generate large-amplitude, quasi-stationary waves (Hoffmann et al., 2013; Kaifler et al., 2020; Liu et al., 2014; Lund et al., 2020).

The vertical propagation of these waves is, however, strongly controlled by the background winds (Dong et al., 2018; Dong et al., 2021b; Dong et al., 2022; Heale et al., 2020a; Heale et al., 2020b). During austral winter, the stratospheric polar-night jet (westerlies) provides favorable propagation conditions that allow mountain waves to reach high altitudes, whereas during summer, easterly or weak winds create critical-level filtering that suppresses upward propagation (Sato et al., 2009). This seasonal "vertical filtering" implies that only during specific seasons—or sporadic episodes with favorable wind conditions—can lower-atmospheric disturbances reach the mesosphere and lower thermosphere (MLT), thereby establishing dynamical coupling between atmospheric layers.

Observational studies increasingly reveal this vertical coupling using combinations of satellite and ground-based instruments. Satellite sounders such as the Atmospheric Infrared Sounder (AIRS) aboard NASA's Aqua satellite provide global, three-dimensional temperature fields sensitive to GWs in the 20–60 km range, with horizontal wavelength resolution down to ~50 km (Hoffmann and Alexander, 2009; Wright et al., 2017; Hindley et al., 2020). AIRS observations have mapped global GW distributions and identified prominent hotspots, including the Southern Andes and the adjacent Drake Passage, where momentum fluxes can exceed 80–100 mPa near 30 km altitude (Wright et al., 2017). Nevertheless, satellite measurements have intrinsic observational filters: the coarse vertical resolution and fixed local-time sampling of infrared nadir sounders such as AIRS render them less sensitive to short-vertical-wavelength and high-frequency waves, leading to systematic underestimation of total GW momentum and energy fluxes (Franco-Diaz et al., 2024).

In contrast, ground-based lidars provide high-resolution vertical profiles of temperature and wind, capable of directly resolving small-scale structures and breaking processes that satellites cannot detect (Kaifler et al., 2020). Rayleigh and sodium (Na) lidars have been extensively used at mid- and high-latitude sites to monitor mesospheric dynamics, often revealing strong, localized wave activity, instabilities, and turbulence layers. For example, Cao et al. (2016) revealed a gravity wave reflection and refraction event that resulted in vertical wind oscillations exceeding 10 m/s. Such a complex process could only be quantified with ground-based measurement such as the Na lidar at the Andes Lidar Observatory (ALO). During an intense mountain-wave event over Tierra del Fuego (54°S), lidar observations recorded temperature perturbations exceeding 80 K and momentum fluxes greater than 100 mPa, demonstrating the extraordinary energy input from orographic sources into the stratosphere (Kaifler et al., 2020). Such observations highlight the value of integrating satellite and lidar datasets to investigate GW vertical coupling.

Long-term climatologies derived from both satellite and lidar datasets have shown pronounced seasonal modulations in GW activity across the stratosphere and mesosphere (Wright et al., 2017; Hindley et al., 2020; Sato et al., 2009). At polar and sub-polar latitudes, lidar measurements (e.g., at the South Pole and Rothera) report substantially higher GW potential energy in winter than in summer, which is consistent with enhanced source activity and more favorable propagation conditions (Sato et al., 2009). Similarly, satellite climatologies display winter maxima in GW momentum fluxes at mid- and high latitudes (Wright et al., 2017). Mid-latitude sites are comparatively quiescent in summer but can experience episodic high-amplitude GW events associated with convection or jet-front systems (Franco-Diaz et al., 2024). Such intermittent bursts can contribute significantly to the local momentum budget, sometimes rivaling wintertime values. Overall, the Southern Hemisphere mid-latitudes exhibit the strongest GW activity during austral winter, in agreement with theoretical and numerical studies of orographic forcing and stratospheric filtering (Sato et al., 2009). Additionally, related high-latitude mesospheric observations also demonstrate pronounced year-to-year variability in short-period GW activity and show that critical-level filtering associated with variability in the stratospheric polar vortex can strongly modulate the transmitted wave field (Mandal et al., 2025).

In addition to observational advances, high-resolution numerical simulations have begun to capture the full life cycle of gravity waves, including their breaking and the subsequent generation of secondary waves. Modeling studies have demonstrated that primary mountain waves often encounter critical layers in the mesosphere, leading to localized instability and turbulent breakdown (Heale et al., 2020a; Dong et al., 2022). Idealized modeling has demonstrated that breaking or strongly dissipating primary GWs can excite secondary waves with a broad range of horizontal and vertical scales and intrinsic frequencies. In some nonlinear scenarios, small-scale secondary waves exhibit shorter horizontal and vertical wavelengths and higher intrinsic frequencies than the primary waves (e.g., the fast-moving acoustic GWs generated by strong primary GW breaking) (Dong et al., 2020; Fritts et al., 2020; Lund et al., 2020). In contrast, secondary waves excited by large-scale GW "pseudomomentum deposition" or self-acceleration (Dong et al., 2020; Lund et al., 2020) or by localized body forces can have much larger horizontal scales than their progenitors (Vadas et al., 2018). These secondary waves can transport momentum fluxes comparable to, or even exceeding, those of the parent wave at its breaking altitude, effectively extending the reach of orographic forcing far above the primary dissipation region. Such multi-stage processes—including wave breaking, secondary-wave generation, and nonlinear mean-flow interactions—are now recognized as crucial components of vertical coupling between the lower and upper atmosphere (Fritts et al., 2020; Lund et al., 2020).

Over the Southern Andes, recent high-resolution observations and modeling have provided detailed case studies of GW sources, propagation, and breaking. Krasauskas et al. (2023) combined GLORIA and ALIMA measurements with ray tracing to document oblique propagation and strong horizontal refraction, leading to substantial meridional redistribution of momentum. Gisinger et al. (2022) used Rayleigh lidar and ECMWF IFS simulations in the lee of the Andes to relate middle-atmosphere temperature biases and intermittency to gravity-wave-driven variability. Noble et al. (2024) applied a three-dimensional (3D) AIRS GW retrieval together with backward ray tracing to map wintertime stratospheric GW sources and their relation to the polar-night jet. Alexander et al. (2025) analyzed SOUTHTRAC flight data and WRF simulations to show how strong mountain waves can self-induce attenuation and partial breaking near the

stratopause, generating secondary modes in the lower mesosphere. In the present study, we complement these event-based and regional analyses by focusing on the multi-year seasonal relationship between stratospheric GW activity observed by AIRS and mesospheric perturbations observed by the Na lidar at ALO. In this study, we test the hypothesis that stratospheric gravity waves observed by AIRS are directly coupled to mesospheric wave and instability signatures detected by lidar, and that this coupling is primarily modulated by seasonal variations in the background winds. We first summarize the observations and analysis methods (Section 2). We then present a case study linking an AIRS-observed wave field to concurrent mesospheric perturbations detected by lidar, followed by seasonal statistics demonstrating coherent AIRS–lidar variability and the controlling influence of background winds (Section 3). Finally, we discuss the implications for vertical GW coupling in Section 4.

2 Methodology

To investigate the vertical coupling of GW dynamics over the Southern Andes, we implement a multi-instrument observational approach that integrates satellite-based temperature perturbations from the AIRS with ground-based Na lidar measurements from the ALO. This combined framework enables a comprehensive examination of GW behavior from the lower stratosphere to the mesopause region, providing both the large-scale horizontal context from AIRS and the high-resolution vertical and temporal detail from lidar observations.

The AIRS instrument aboard NASA's Aqua satellite provides global measurements of temperature perturbations in the stratosphere and lower mesosphere (20–60 km), resolving horizontal wavelengths down to ~50 km. These data allow characterization of GW sources, horizontal propagation, and large-scale spatial distributions of wave energy and momentum fluxes. In contrast, the ALO Na lidar measurements (85–100 km) offer high-precision, high-cadence temperature profiles that capture fine-scale wave dynamics, breaking, and instability processes occurring near the mesopause. Despite the different observational filters and sensitivities of the two instruments—AIRS being more responsive to large-scale, lower-frequency waves and the lidar to small-scale, high-frequency perturbations—together they provide a complementary perspective on GW evolution across more than 70 km of altitude.

2.1 AIRS observations

In this study, we use the 3D spectral analysis method introduced by Wright et al. (2017), which is based on a generalized multidimensional extension of the Stockwell transform (ST). This method enables the automatic detection and characterization of atmospheric GWs in 3D temperature fields and allows for the retrieval of a wide range of wave parameters, including amplitudes, wavenumbers, phase and group velocities, intrinsic frequencies, and momentum fluxes.

The analysis utilizes three-dimensional stratospheric temperature fields derived from the AIRS aboard NASA's Aqua satellite. The retrievals are based on the 4.3- and 15-μm CO_2 bands following the method of Hoffmann and Alexander (2009), providing data with a vertical range of 20–60 km and vertical resolution between 7 and 15 km depending on height. Retrieval noise varies between 1 and 2 K in the same altitude range. Horizontal resolution varies from approximately 13.5 km at nadir to 40 km near the scan edges, corresponding to the size of individual AIRS footprints.

Temperature perturbations $T'(x,y,z)$ associated with gravity waves are obtained by detrending each across-track scan using a fourth-order polynomial at every height level, effectively removing large-scale background variability and planetary wave signals. The detrended temperature fields are then interpolated onto a regular spatial grid of $64\times128\times16$ points in the across-track, along-track, and vertical directions, respectively, to optimize the subsequent fast Fourier transform (FFT) operations used in the 3D ST computation.

To mitigate spectral leakage caused by the exponential increase in wave amplitude with height, the data are scaled by $\exp[-(z-z_0)/2H]$, where $z_0 = 41$ km is the reference altitude and $H = 7$ km is the atmospheric scale height.

The multidimensional ST provides a localized spectral decomposition of a field $h(\mathbf{x})$ in both spatial and wavenumber domains. The N-dimensional ST, $S(\boldsymbol{\tau},\mathbf{f})$, is defined in Equation 1:

$$S(\boldsymbol{\tau},\mathbf{f}) = \frac{1}{(2\pi)^{N/2}}\int_{-\infty}^{\infty} h(\mathbf{x})\prod_{n=1}^{N}\left[|f_n|c_n^{-1}\exp\left(-\frac{(x_n-\tau_n)^2 f_n^2}{2c_n^2}\right)\right]e^{-i2\pi\mathbf{f}\cdot\mathbf{x}}\,d\mathbf{x}, \tag{1}$$

where $\boldsymbol{\tau} = (\tau_1,\tau_2,\ldots,\tau_N)$ represents the translation vector, $\mathbf{f} = (f_1,f_2,\ldots,f_N)$ the spatial frequencies, and c_n the localization parameters controlling the trade-off between spatial and spectral resolution. For AIRS analysis, Wright et al. (2017) adopted $(c_x,c_y,c_z) = (0.25,0.25,0.1)$ to account for the larger vertical extent of wave structures relative to horizontal scales.

At each voxel, the spectral peak in the local (f_x,f_y,f_z) domain identifies the dominant wave component. The corresponding amplitudes and wavenumbers are stored as $A(x,y,z)$ and (k,l,m), representing zonal, meridional, and vertical wavenumbers, respectively.

Because the ST operates on finite wave packets, the retrieved amplitudes are systematically underestimated due to spectral leakage. To correct for this, an empirical amplitude restoration factor ξ is derived by comparing the 3D Fourier transforms of the original temperature perturbation field $T'(x,y,z)$ and the ST reconstruction $R(x,y,z)$, as shown in Equation 2:

$$\xi = \text{median}\left(\frac{|\mathcal{F}[T'(x,y,z)]|}{|\mathcal{F}[R(x,y,z)]|}\right). \tag{2}$$

The corrected amplitude field is then obtained as $\xi A(x,y,z)$. For each AIRS granule, the empirical amplitude-restoration factor ξ is computed as the median ratio of the 3D Fourier amplitude spectra of the original detrended temperature perturbations and ST reconstruction over the range of resolved wave numbers. Applying ξ rescales the ST amplitudes so that the leading spectral peaks closely match those of the full-field Fourier transform. Tests across a wide variety of AIRS wave fields show that this procedure recovers the dominant spectral amplitudes to within approximately 10% on average.

Under the mid-frequency approximation, the vertical flux of horizontal momentum $\mathbf{M} = (M_z,M_m)$ is estimated using Equation 3,

following the study by Ern et al. (2004):

$$[M_z, M_m] = \frac{\rho}{2}\frac{(k,l)}{|m|}\left(\frac{g}{N_B}\right)^2\left(\frac{T'}{T}\right)^2, \quad (3)$$

where N_B is the Brunt–Väisälä frequency, ρ and T are the mean atmospheric density and temperature, respectively, and g is the acceleration due to gravity. Because the method provides direct estimates of k, l, and m, the resulting momentum flux represents an actual value rather than a lower bound, as is typical in earlier 2D satellite analyses.

To resolve the 180° ambiguity in the wavevector, it is assumed that the GWs propagate vertically upward, implying $m < 0$. Recent high-resolution lidar measurements demonstrate that downward-propagating GWs constitute a substantial fraction of the mesospheric wave population, typically contributing on the order of one-third of resolved wave packets (Wing et al., 2025). Our "transmission-window" framework focuses on upward-propagating waves between the AIRS sensitivity layer (20–60 km) and the mesosphere (Sato et al., 2009). This assumption is adopted for conceptual simplicity and does not imply that downward-propagating components are negligible in the mesosphere.

The analysis was implemented on desktop computing hardware with each AIRS granule processed individually and then combined into composite climatologies. Granule boundaries were overlapped by half-length during processing to minimize truncation effects at edges.

2.2 Na lidar observations

The Na lidar observations used in this study were conducted at the ALO, located at Cerro Pachón, Chile (30.3°S and 70.7°W), a region characterized by strong and frequent GW activity. The ALO Na lidar system is equipped with a high-power transmitter and efficient receiver optics, achieving a large power-aperture product of 0.66 W m^{-2} (Liu et al., 2016). Combined with the high-altitude, clear-sky conditions of the Andes, this configuration enables high-quality temperature and horizontal wind measurements in the mesopause region (Guo et al., 2020).

The lidar measurements used here cover 244 nights between May 2014 and September 2019, totaling 2,170 h of observations (Yang and Liu, 2022). During standard operations, the laser beam was directed toward zenith (Z) and 20° off-zenith toward the east (E) and south (S) in a zenith-south-zenith-east sequence, producing a temporal resolution of approximately 4 min for complete temperature and horizontal and vertical wind retrievals. On some nights, only the zenith beam was operated, providing higher-temporal-resolution (~1 min) vertical wind and temperature measurements.

Photon counts were recorded with 6-s temporal and 25-m range resolutions and then binned to 60-s and 500-m resolutions to derive temperature and line-of-sight (LOS) wind profiles. At these resolutions, the typical root-mean-square (rms) uncertainties in the 85–100 km altitude range are less than 2 K for temperature and 6 m s^{-1} for horizontal wind components. Measurements exceeding 10 K (temperature) or 20 m s^{-1} (horizontal wind) uncertainty were excluded, retaining approximately 95% of data. For subsequent analysis, temperature and wind profiles were interpolated to uniform vertical (500 m) and temporal (0.1 h) grids, which could resolve perturbations as small as 1 km and 12 min.

To isolate GW-induced perturbations, each temperature profile was decomposed into mean and fluctuating components, as shown in Equation 4:

$$T'(z,t) = T(z,t) - \overline{T}(z,t), \quad (4)$$

where the overbar denotes the background field obtained using a low-pass filter. We remove tidal and planetary-wave variability, as well as mean backgrounds, by applying a two-dimensional low-pass filter in time and altitude, yielding a background field $\overline{T}(z,t)$ and perturbation $T'(z,t)$. With the adopted filter scales, the resulting perturbations are primarily sensitive to GW intrinsic periods between roughly 5 and 360 min (0.08–6 h); slower tides and planetary waves are strongly attenuated. This ensures that the lidar variance is computed over a GW band comparable to the AIRS sensitivity range. Vertical profiles were then interpolated onto uniform 500 m altitude grids and smoothed with a 1-km vertical running mean to suppress photon noise while preserving small-scale GW structures.

3 Results

Figure 1 illustrates a representative event during 3–4 August 2019. The top row shows time–height sections of lidar-derived u', v', and T' between 80 and 100 km. We distinguish the band-pass GW component (primarily 5–360 min) from the low-frequency background flow (periods > 360 min, including tidal and planetary-wave variability as well as the mean). The background wind is the low-pass (>360 min) component of the Na-lidar winds in the mesosphere. During this event, the background flow is predominantly westerly (not shown here), so the observed downward phase tilt is interpreted as upward energy propagation relative to the mean/background wind. The bottom panels show colocated AIRS 3-D temperature-perturbation fields on consecutive overpasses, revealing quasi-stationary, large-amplitude wave packets over the Southern Andes/Drake Passage. This example is intended to demonstrate the temporal coincidence and general spatial alignment of strong stratospheric GW activity with active mesospheric perturbations above ALO. From the multi-year AIRS climatology in Figure 2, the daily-mean GW amplitudes and momentum fluxes during 3–4 August 2019 lie in the upper portion of the winter distribution. The event is representative of a relatively strong but not extreme wintertime mountain-wave episode, with amplitudes roughly a factor of three to four larger than the concurrent winter mean.

Figure 2 summarizes the seasonal variation of GW activity in the stratosphere as observed by AIRS over the Southern Andes, based on the multi-year climatological mean. The AIRS data were analyzed on a daily basis using only nighttime retrievals from the descending orbit, which employ both the 4.3-μm and 15-μm CO_2 channels. This selection minimizes nonlocal thermodynamic equilibrium (non-LTE) and solar-excitation effects and ensures consistent temperature retrieval quality across seasons. Two GW parameters are shown: the mean perturbation amplitude (Figure 2a) and the mean total momentum flux (Figure 2b). Both parameters exhibit a pronounced

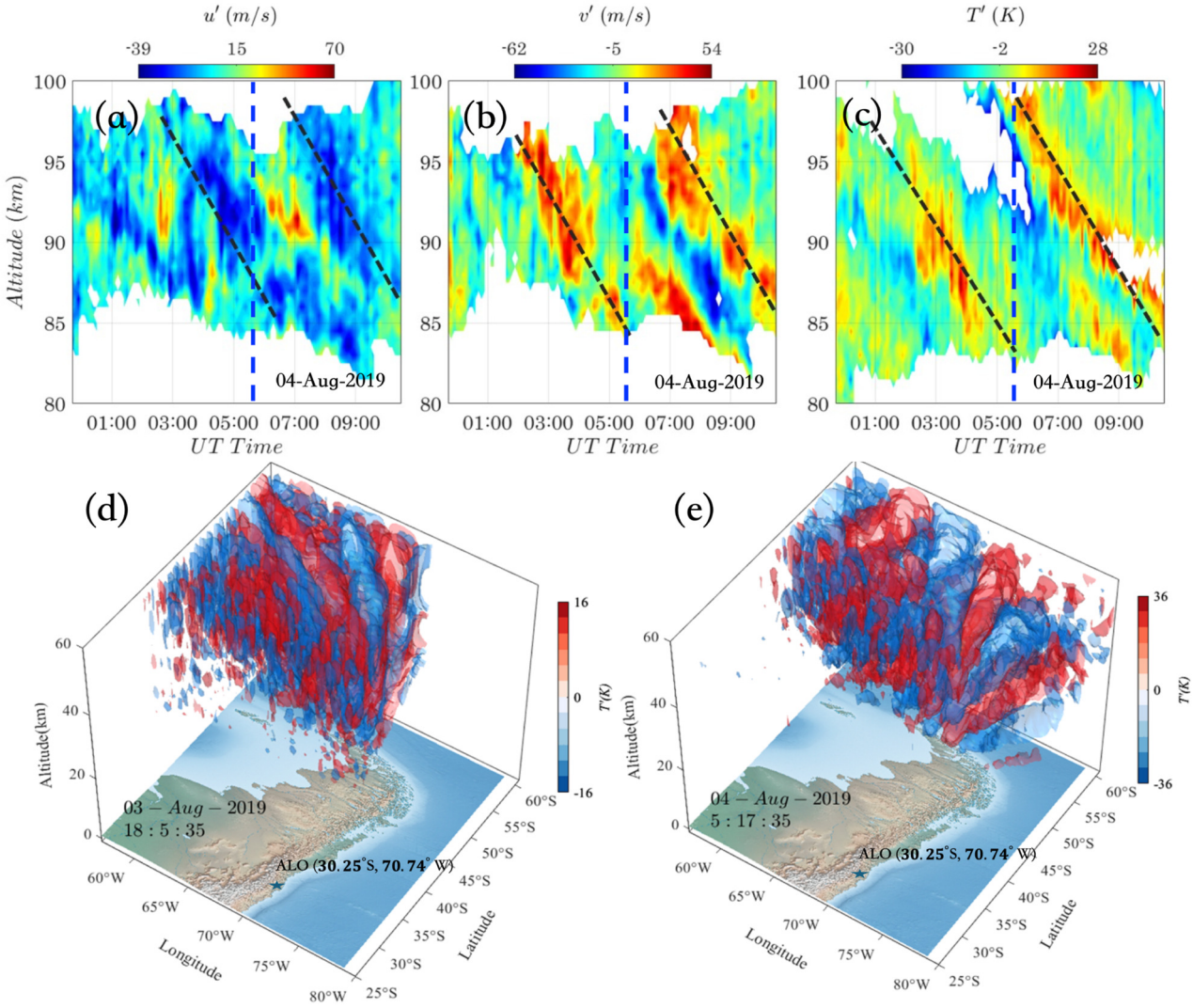

FIGURE 1
(top: **a–c**) Time–altitude cross sections of zonal wind perturbation (u': **(a)** meridional wind perturbation (v') **(b)** and temperature perturbation (T'), **(c)** with periods shorter than 6 h, derived from sodium (Na) lidar observations at the Andes Lidar Observatory (ALO; 30.25°S and 70.74°W) on 4 August 2019. (bottom: **d,e**) Three-dimensional temperature perturbation (T') fields retrieved from Atmospheric Infrared Sounder (AIRS) observations on 3 August 2019 **(d)** and 4 August 2019 **(e)**. The stars in panels d and e indicate the location of the Andes Lidar Observatory, and the vertical blue line in the time–series panel marks the time of the second AIRS overpass (05:17:35 UT), facilitating comparison between the satellite and lidar observations. The combined views from AIRS and Na lidar show an example of GW events simultaneously captured in both the stratosphere and the mesosphere.

seasonal cycle, characterized by a broad maximum during the austral winter months and a minimum in summer. The winter enhancement is clearly evident: for example, the total momentum flux increases rapidly beginning in May, reaches its maximum in July–August, and then decreases toward October, while remaining close to its annual minimum during the summer months of December–February. The multi-year mean (blue line) indicates that on average, GW amplitudes and momentum fluxes from May through September are approximately four to five times larger than their summer minima.

The gray shaded envelopes in Figure 2 represent the interannual variability, defined by the 16th–84th percentile range of daily values across all years for each day of the year, after applying a 7-day temporal smoothing. This percentile-based representation characterizes the typical year-to-year spread of GW activity without assuming a Gaussian distribution. The width of the shaded bands indicates that the timing and magnitude of the winter peak vary substantially from year to year, although the overall seasonal pattern remains robust. The observed seasonal modulation is consistent with the well-known behavior of orographic gravity waves. During austral winter, stronger background westerlies and more favorable propagation conditions allow larger-amplitude waves generated by flow over the Andes to propagate upward into the stratosphere, leading to enhanced GW amplitudes and momentum transport. In contrast, summer conditions tend to suppress or dissipate many mountain waves, resulting in much weaker GW activity. Despite notable interannual variability, the persistent wintertime enhancement underscores the robust seasonal coupling of tropospheric forcing and stratospheric GW dynamics

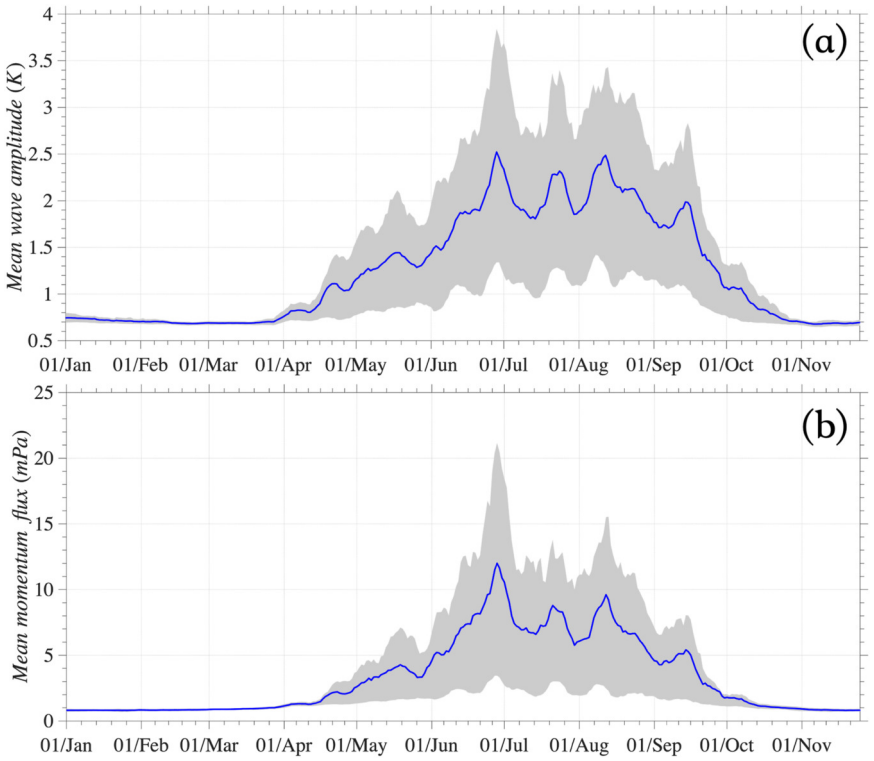

FIGURE 2
Seasonal variations of zonal-mean GW parameters derived from AIRS observations over the Southern Andes at an altitude of 40 km. Panel **(a)** shows the mean GW amplitude, and panel **(b)** shows the mean total momentum flux. The solid blue lines denote the multi-year climatological mean computed from all available years in the analysis record (after standard quality control). The gray shaded envelopes represent the interannual variability, defined by the 16th–84th percentile range of the daily values across all years for each day of year, after applying a 7-day smoothing. This percentile-based range characterizes the typical year-to-year spread of GW activity without assuming a Gaussian distribution.

over the Southern Andes. In this paper, we adopt a simple calendar-based definition of austral winter (June–August) and summer (December–February) when discussing seasonal behavior, both because the lidar sampling is intermittent and because our focus is on robust seasonal patterns rather than detailed regime classification. Future studies with denser ground-based coverage could beneficially define "winter" and "summer" based on the onset and breakdown of the stratospheric jet.

To compare satellite and ground-based perspectives on sub-seasonal time scales, we constructed composite-year monthly means from all available observations and restricted AIRS sampling to months with lidar coverage. Figure 3 presents AIRS temperature variance (black, right axis) alongside Na-lidar temperature variance (red). To evaluate the robustness of the seasonal climatology, sampling uncertainties were estimated for both instruments based on interannual variability rather than short-term fluctuations. For each calendar month, monthly mean values were first calculated separately for each year and then averaged to construct the climatological seasonal cycle. The associated uncertainty was quantified as the standard deviation of the calendar-month means across all available years, thereby representing month-to-month variability in the climatological sense. For the Na lidar, temperature variance was computed for each month in each year using all nights with usable observations, and the spread of these monthly means provides a measure of interannual variability in GW activity. For AIRS, monthly mean temperature perturbation amplitudes were derived in an analogous manner using only months with concurrent lidar observations, ensuring consistent temporal sampling between the two datasets. The resulting uncertainties are shown as shaded envelopes ($\pm 1\sigma$) in Figure 3. The shaded uncertainty ranges are substantially smaller than the contrast between austral-winter and summer conditions, confirming that the pronounced wintertime enhancement in GW activity is a robust and statistically significant feature in both the lidar and AIRS observations. Both observations display pronounced austral-winter enhancements, indicating that intensified lower-stratospheric GW activity is communicated upward and manifests as enhanced mesospheric perturbations during the same season.

ERA5 reanalysis winds (Hersbach et al., 2020) averaged over the Andes (Figure 4) clarify the following mechanism: low-level westerlies at ~2 km persist year-round, implying continuous orographic forcing, whereas the stratosphere exhibits a strong winter jet and marked seasonal reversals. Thus, mesospheric GW visibility is governed primarily by propagation rather than generation—winter jets open vertical "transmission windows" that allow mountain waves to reach (and dissipate within) the upper mesosphere, whereas summer conditions favor reflection or critical-level absorption below.

Returning to Figure 3, we now examine in more detail how the composite seasonal cycles in AIRS and lidar variances compare

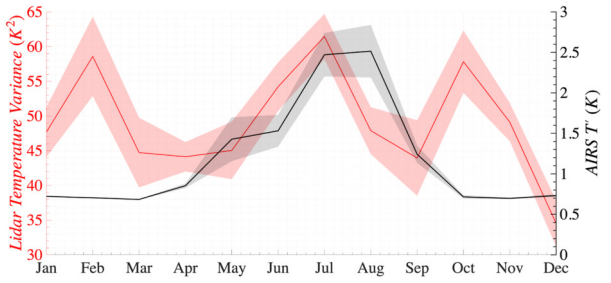

FIGURE 3
Seasonal variation of GW-band activity (T_{GW} < 6 h) over the Southern Andes derived from Na-lidar and AIRS observations. The red curve shows the monthly mean lidar temperature variance (T'^2) at the selected altitude, whereas the black curve represents the AIRS-derived temperature perturbation amplitude averaged over the 20–60 km altitude range. Shaded regions indicate the ±1σ uncertainty of the monthly means, estimated from the month-to-month variability of the corresponding calendar-month averages across all available years (2014–2020). For AIRS, monthly means and uncertainties are derived in an analogous manner using only months with concurrent lidar observations, ensuring temporal consistency between the two data sets. Both lidar and AIRS exhibit pronounced austral-winter (June–August) enhancements, indicating strong seasonal modulation of GW activity and coherent vertical coupling between the stratosphere and mesosphere.

across the different intrinsic-period bands. A notable difference between the observation platforms is the seasonal peak structure: the Na-lidar composites exhibit three discernible maxima—a broad winter enhancement (May–August), a spring shoulder (October), and a secondary summertime peak (February), whereas AIRS shows a single, broader mid-winter maximum. The additional peaks in the Na-lidar seasonal variance (e.g., near February and October) do not necessarily imply a contradiction with the AIRS stratospheric composite as the two diagnostics sample different altitude ranges and different portions of the GW spectrum. The lidar metric emphasizes GW-band variability (T_{GW} = 5–360 min; i.e., T_{GW} < 6 h) at a fixed mesospheric altitude, whereas the AIRS product represents temperature perturbation amplitudes averaged over a broad 20–60 km stratospheric layer and is subject to substantial vertical smoothing and reduced sensitivity to short vertical wavelengths.

One plausible explanation for the additional peaks observed in the Na lidar seasonal cycle is the presence of seasonal transmission windows during transitional periods. Over the Andes, near-surface westerlies persist year-round, sustaining continuous orographic GW generation, whereas the stratospheric jet strengthens in winter and weakens or reverses in summer (Figure 4). This zonal wind acts as a seasonal gate: during winter, stationary mountain waves experience a tailwind and can propagate well above 30 km; during summer, easterlies impose critical levels that block upward propagation below ~20–30 km (Fritts and Alexander, 2003; Sato et al., 2009). As the stratospheric circulation evolves into and out of austral winter, transient shear layers and partial wind reversals can intermittently permit subsets of the GW spectrum—often waves with shorter vertical wavelengths or higher intrinsic frequencies—to propagate upward into the mesosphere (85–100 km). These wave components may not contribute strongly to the AIRS signal, which is vertically averaged over the 20–60-km altitude range and subject to substantial vertical smoothing, but they can, nevertheless, produce enhanced mesospheric temperature variance detectable by the lidar.

A second, closely related contribution arises from wave breaking, dissipation, and secondary GW generation near the mesopause. As primary GWs propagate upward, their amplitudes grow exponentially with decreasing atmospheric density until they reach saturation or instability thresholds, leading to wave breaking, turbulence, and momentum deposition. Lidar measurements at ALO have documented enhanced instability occurrence and dissipative fluxes in the mesopause region during winter, which is consistent with active breaking (Guo et al., 2020; Yang and Liu, 2022). These processes can excite secondary GWs with different spatial scales and intrinsic frequencies from those of the primary waves. Moreover, breaking and associated imbalances can radiate secondary GWs with shorter vertical scales and different phase speeds (Fritts and Alexander, 2003; Sato et al., 2009; Dong et al., 2023). The Na lidar is particularly sensitive to such small-scale fluctuations and instability signatures in the mesopause region, whereas AIRS primarily samples the wave field at lower altitudes before significant dissipation occurs. Consequently, the lidar seasonal cycle reflects not only the upward transmission of primary waves but also the cumulative effects of mesospheric dissipation and secondary-wave radiation, which can introduce additional structure and shift or sharpen seasonal peaks relative to the stratospheric AIRS signal.

To assess whether the late spring (February) and summer (October) mesospheric variance maxima correspond to systematic spectral changes in the lidar-resolved small-scale wave field, we performed a simple vertical-wavenumber spectral analysis of the Na-lidar temperature perturbations. We computed one-sided power spectral densities of nightly mean $T'(z)$ profiles between 85 and 100 km after linear detrending. Monthly mean spectra were obtained by averaging across all available nights in each month, and uncertainties were estimated from the night-to-night variability. Figure 5 shows that the mesospheric spectra are approximately power-law over vertical wavelengths of order 1–10 km. Across all months, the spectra exhibit broadly similar shapes, with power decreasing monotonically toward higher vertical wavenumbers. Over intermediate wavenumbers (m ~ 0.3–2 rad km^{-1}), the spectra follow an approximate −5/3 power-law slope, which is consistent with saturated or turbulence-influenced mesospheric GW spectra. Seasonal variability is expressed through changes in both spectral amplitude and spectral slope. Austral winter months (July–August) show enhanced spectral power across a broad range of vertical wavenumbers, corresponding to increased GW activity under favorable propagation conditions. Secondary enhancements in spectral power are evident during late spring and summer, coincident with the mesospheric variance shoulder peaks identified in the lidar statistics. The spectral power evolution indicates that mesospheric GW variability is associated with distinct vertical-scale distributions in different seasons. The enhanced variability reflects amplitude modulation of an otherwise persistent GW spectrum. Additionally, Figure 5 reveals modest month-to-month shifts in the relative power between shorter and longer vertical wavelengths, indicating scale-dependent modulation of GW activity.

Taken together, the multiple peaks in lidar variance are consistent with a framework in which primary mountain

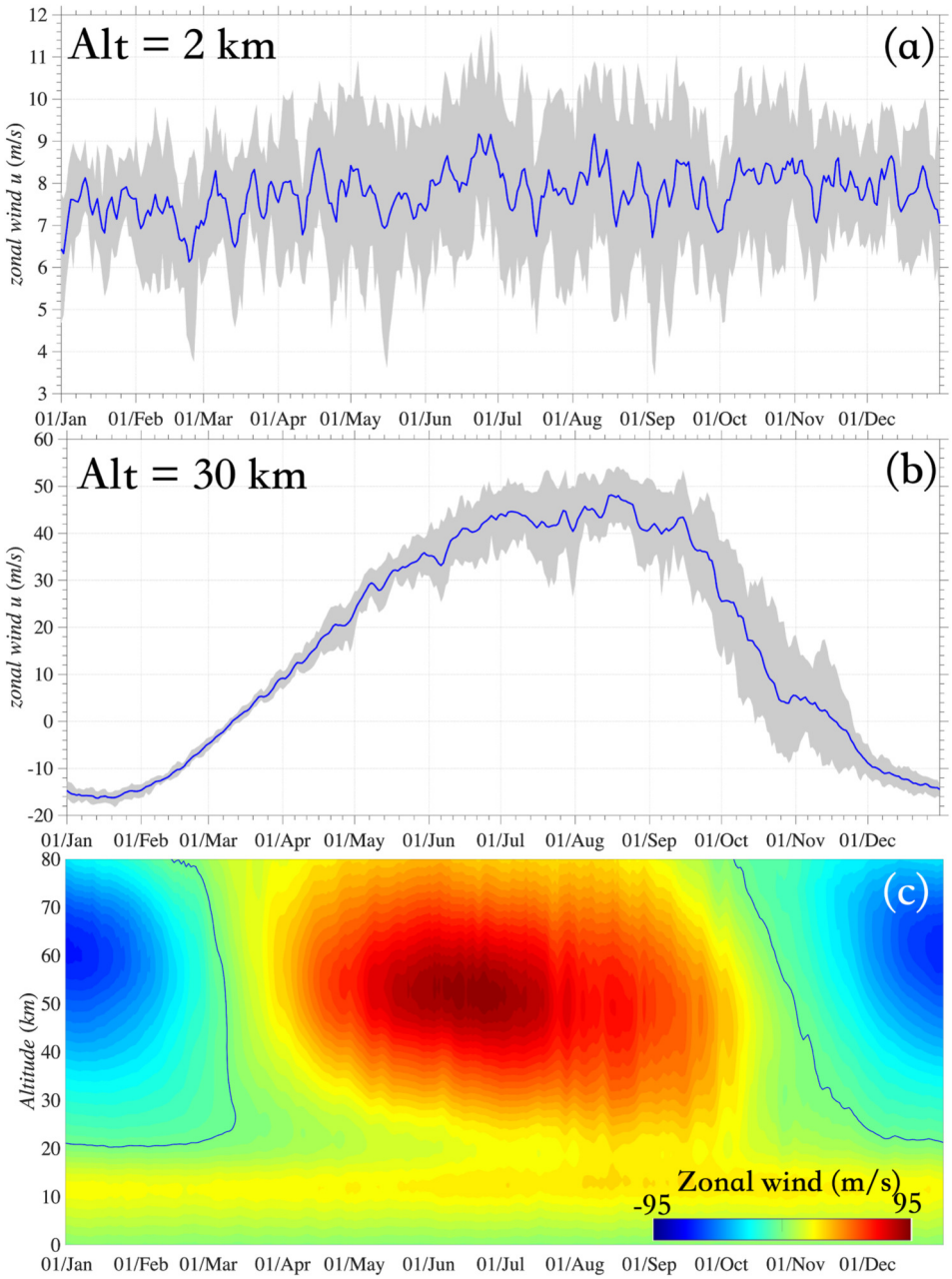

FIGURE 4
Seasonal variations of zonal winds over the Southern Andes derived from ERA5 reanalysis. **(a)** Time series of daily zonal wind speed at 2 km altitude and **(b)** at 30 km altitude, shown as climatological seasonal cycles. The blue curve denotes the multi-year mean, whereas the gray shaded envelopes represent the interannual variability, defined by the 16th–84th percentile range of the daily values across all years for each day of year, after applying a 7-day smoothing. **(c)** Time–altitude cross section of the zonal wind component averaged over the Andes region (70–75°W, 30–40°S); the blue contour indicates the zero zonal wind ($u = 0$), marking the transition between easterly and westerly flow. Near the surface, zonal winds exhibit relatively weak seasonal variability, whereas in the stratosphere and mesosphere, a pronounced seasonal cycle emerges, with enhanced westerlies during austral winter that favor upward GW propagation.

waves experience seasonally varying transmission and dissipation and in which breaking and instabilities near the stratopause and mesosphere generate secondary waves and local body-force-driven responses [e.g., Alexander et al. (2025); Vadas et al. (2018); Dong et al. (2020); Dong et al. (2021a); Fritts et al. (2020); Lund et al. (2020)]. In this framework, the side peaks may reflect transitions between regimes dominated by primary waves and those in which secondary and locally generated waves contribute more strongly to the mesospheric variance. At the same time, the present observations do not allow unambiguous identification of the sources of the lidar side peaks. Resolving their origin will require targeted dynamical analyses that explicitly link wave generation, transmission, and dissipation processes across altitudes. As a next step, we plan to conduct 1-year high-resolution two-dimensional numerical simulations over the ALO region, using time- and spatially varying background fields constrained

by WACCM-X, to investigate the potential sources and mechanisms responsible for the observed side peaks.

4 Discussion and summary

Our joint AIRS–lidar analysis demonstrates that vertical coupling over the Southern Andes is primarily governed by seasonally varying propagation conditions rather than by source intermittency. The AIRS climatology exhibits a broad austral-winter maximum in wave amplitude and momentum flux (Figure 2), whereas composite monthly means reveal that AIRS and lidar amplitudes co-vary seasonally across short- and medium-period bands (Figure 3). It shows that when wintertime winds open a vertical "transmission window," orographic wave energy can be efficiently communicated to the mesopause, where waves saturate and break (Fritts and Alexander, 2003; Sato et al., 2009). Consistent with earlier AIRS analyses at Southern Hemisphere orographic hotspots, correlations between GW activity and background winds are much larger at stratospheric observational levels (~30–35 km) than with low-level (2 km) winds, indicating that mesospheric visibility is controlled primarily by propagation rather than generation (Hoffmann et al., 2016). Together with the ERA5 wind structure over the Andes (Figure 4), this supports the interpretation that the mesospheric signal is chiefly controlled by background-wind filtering aloft rather than by variability in low-level forcing, which remains strong year-round over the Andes. We also note that AIRS' observational filter limits sensitivity to short-vertical-wavelength, high-frequency waves due to its vertical resolution (7–15 km) and sampling, so the absence of an AIRS signal—especially under weak stratospheric winds—does not imply the absence of shorter-scale GWs. In our framework, the AIRS–lidar correspondence, therefore, represents the subset of long-vertical-wavelength waves that successfully traverse the stratosphere and reach the mesopause, whereas shorter-scale components may be under-sampled by AIRS but still be manifested in the lidar. As a result, only a subset of waves with suitable scales, orientations, and propagation paths will be simultaneously visible to both instruments, and the effective forcing region for the lidar may be horizontally displaced from the Andes by hundreds of kilometers due to oblique propagation and horizontal refraction [e.g., Vadas et al. (2018); Noble et al. (2024)].

Our inference that propagation conditions dominate the seasonal cycle is based primarily on the ERA5 wind climatology (Figure 4) together with the coherent wintertime enhancement observed in both AIRS and lidar (Figures 2, 3); Figure 5 provides additional context by showing that the mesospheric variability is largely broadband, with only modest scale-dependent modulation within the resolved λ_z range. Additionally, the present analysis cannot directly follow individual waves from the lower atmosphere to the mesopause and therefore does not provide a fully height-resolved budget of GW momentum flux. Such detailed diagnostics have been obtained in recent SOUTHTRAC studies that combine airborne observations and high-resolution modeling to track individual wave packets and their vertical wavelength evolution [e.g., Alexander et al. (2025); Krasauskas et al. (2023); Gisinger et al. (2022); Noble et al. (2024)]. Our contribution is complementary: by combining nearly two decades of AIRS data with several years of Na lidar observations, we demonstrate that the seasonal cycle of mesospheric perturbations at ALO is closely aligned with the seasonal modulation of stratospheric GW activity over the Andes. This seasonal co-variability supports the broader picture of strong vertical coupling over this hotspot, whereas detailed vertical transmission and spectral evolution are addressed by the aforementioned case study and modeling investigations.

Our key findings can be summarized as follows:

- Concurrent AIRS and lidar observations during winter document efficient vertical coupling from the lower stratosphere to the mesopause.
- AIRS shows robust austral-winter enhancements in amplitude and momentum flux over the Southern Andes.
- Composite AIRS and lidar amplitudes peak together in winter for short- and medium-period bands, indicating seasonally controlled upward communication of GW activity.
- ERA5 winds confirm year-round low-level westerlies but strong seasonal modulation aloft, identifying propagation—rather than generation—as the primary control on mesospheric GW visibility and dissipation.

The results support a simple conceptual model: (i) *generation*—persistent near-surface westerlies over the Andes continually excite primary mountain waves; (ii) *propagation*—strengthened stratospheric jets during austral winter reduce critical-level filtering, enabling efficient upward transmission; in contrast, summer easterlies block much of the wave spectrum; (iii) *dissipation*—near the mesopause, decreasing density amplifies wave amplitudes until saturation and turbulence occur, producing measurable sensible and enthalpy fluxes, as well as mesospheric cooling (Guo et al., 2020; Yang and Liu, 2022); and (iv) *secondary radiation*—imbalances and body forces associated with breaking generate secondary GWs with distinct scales and phase speeds, redistributing momentum and energy above and away from the primary breaking region (Heale et al., 2020a; Fritts and Alexander, 2003). This framework explains why the lidar exhibits structured peaks (early-winter, mid-winter, and spring shoulders), whereas AIRS retains a single broad mid-winter maximum. AIRS senses the GW spectrum as it propagates through 20–60 km, where observational filtering limits sensitivity to small-scale components (Hoffmann and Alexander, 2009; Hoffmann and Alexander, 2010; Franco-Diaz et al., 2024), whereas the lidar samples the wave field after further spectral reshaping by breaking and secondary-wave generation near 80–100 km.

Differences in instrument sensitivity and sampling naturally yield amplitude offsets and slightly different seasonal structures. AIRS preferentially detects horizontally extensive wave packets and moderate vertical scales, whereas the lidar resolves short-vertical-scale, higher-frequency fluctuations and instability layers (Hoffmann and Alexander, 2009; Wright et al., 2017; Liu et al., 2016). Despite these differences, the coherence observed between AIRS and lidar provides strong support for the utility of combined satellite–lidar analyses when evaluating or tuning GW parameterizations.

Our joint AIRS–lidar analysis supports a source–propagation–dissipation framework in which year-round orographic forcing,

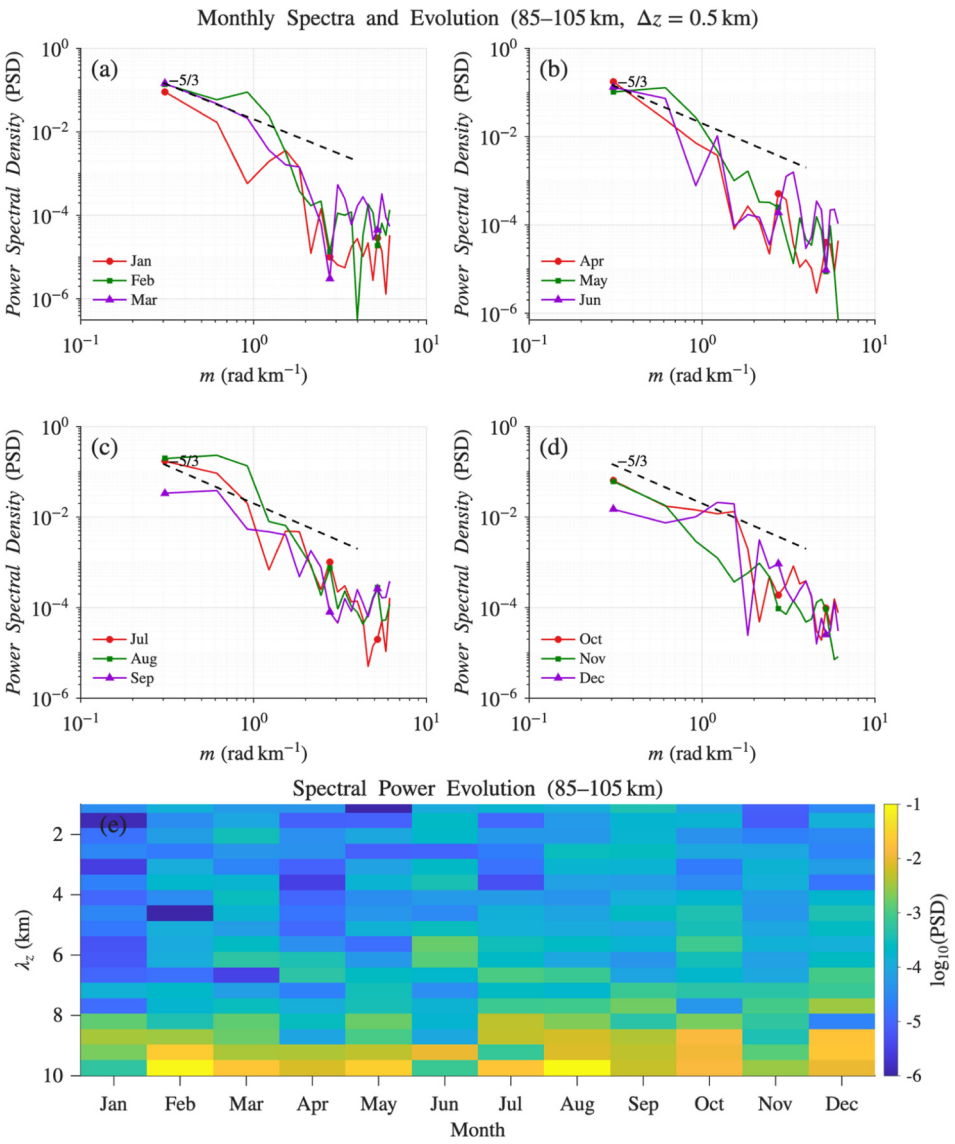

FIGURE 5
(a–d) Monthly mean vertical wavenumber spectra of lidar temperature perturbations in the mesopause region (85–100 km), computed using a vertical resolution of $\Delta z = 0.5$ km. The dashed black line indicates a reference −5/3 power-law slope. **(e)** Seasonal evolution of spectral power as a function of month and vertical wavelength λ_z, shown as $\log_{10}$(PSD). Enhanced spectral power during late austral spring and summer highlights pronounced seasonal variability in mesospheric GW activity.

wintertime transmission through a strengthened stratospheric jet, and mesospheric breaking and secondary-wave radiation shape the seasonal patterns observed at 30–40 km and 85–100 km. Our interpretation that mesospheric GW enhancements at ALO arise from seasonally varying transmission through the stratospheric jet and subsequent breaking near the mesopause is in agreement with detailed case studies of Andes waves during the SOUTHTRAC campaign (Krasauskas et al., 2023; Alexander et al., 2025) and with lidar–model comparisons of temperature variability in the lee of the Andes (Gisinger et al., 2022). Likewise, the strong sensitivity of AIRS-derived GW activity to the structure of the polar-night jet over the Southern Hemisphere, emphasized by Noble et al. (2024), aligns with our finding that mesospheric visibility is governed primarily by propagation conditions aloft rather than variability in low-level forcing.

Remaining uncertainties include (i) imperfect satellite–ground co-location and potential aliasing by fast group velocities or background advection and (ii) differing observational filters that may bias amplitude estimates. Future work will benefit from (a) group-velocity ray tracing or back-trajectory analyses from AIRS 3D fields to the ALO line of sight, (b) joint spectral or bispectral diagnostics to isolate secondary-wave signatures, and (c) targeted high-resolution modeling to link observed instability and fluxes to underlying source spectra and to validate momentum-flux retrievals. Future work will also benefit from combining the 3D AIRS fields with intrinsic-parameter retrievals from high-resolution lidar wave-packet analyses [e.g., Wing et al. (2025)], providing firm

mesospheric starting points for group-velocity ray tracing or back-trajectory calculations down to the stratosphere. Such studies would enable a more direct attribution of observed mesospheric GWs to specific source regions and background-wind environments.

Data availability statement

The datasets presented in this study can be found in online repositories. The names of the repository/repositories and accession number(s) can be found below: http://alo.erau.edu/data/nalidar/ and https://datapub.fz-juelich.de/slcs/airs/gravity_waves/data/projects/wenjun/.

Author contributions

WD: Conceptualization, Data curation, Formal Analysis, Funding acquisition, Investigation, Methodology, Project administration, Resources, Software, Supervision, Validation, Visualization, Writing – original draft, Writing – review and editing. AL: Conceptualization, Data curation, Formal Analysis, Methodology, Writing – review and editing. LH: Conceptualization, Data curation, Formal Analysis, Methodology, Validation, Writing – review and editing. DF: Conceptualization, Investigation, Writing – review and editing. FY: Data curation, Investigation, Methodology, Writing – review and editing. JH: Data curation, Formal Analysis, Writing – review and editing.

Funding

The author(s) declared that financial support was received for this work and/or its publication. This research was supported by NSF Grants (AGS-2327914 and AGS-2017339) and NASA Grant (80NSSC24K0124).

Acknowledgements

The authors gratefully acknowledge Corwin Wright and his team for openly sharing their 3D S–T analysis code. Much of the AIRS data analysis in this study was conducted using their publicly available tools. The code can be accessed at https://github.com/corwin365/MatlabFunctions.

Conflict of interest

Authors WD and DF were employed by Global Atmospheric Technologies and Sciences.

The remaining author(s) declared that this work was conducted in the absence of any commercial or financial relationships that could be construed as a potential conflict of interest.

Generative AI statement

The author(s) declared that generative AI was not used in the creation of this manuscript.

Any alternative text (alt text) provided alongside figures in this article has been generated by Frontiers with the support of artificial intelligence and reasonable efforts have been made to ensure accuracy, including review by the authors wherever possible. If you identify any issues, please contact us.

Publisher's note

References

Alexander, M. J., Gille, J., Cavanaugh, C., Coffey, M., Craig, C., Dean, V., et al. (2008). Global estimates of gravity wave momentum flux from high resolution dynamics limb sounder (hirdls) observations. *J. Geophys. Res. Atmos.* 113, D15S18. doi:10.1029/2007JD008807

Alexander, P., de la Torre, A., Marcos, T., Hierro, R., Kaifler, N., Rhode, S., et al. (2025). Self-induced gravity wave attenuation and breaking with generation of secondary modes in the lower mesosphere during two southtrac flights above the andes. *J. Geophys. Res. Atmos.* 130, e2024JD042981. doi:10.1029/2024JD042981

Cao, B., Heale, C. J., Guo, Y., Liu, A. Z., and Snively, J. B. (2016). Observation and modeling of gravity wave propagation through reflection and critical layers above andes lidar observatory at Cerro Pachón, Chile. *J. Geophys. Res. Atmos.* 121 (12), 737. doi:10.1002/2016JD025173

Chau, J. L., Poblet, F. L., Liu, H., Liu, A., Gulbrandsen, N., Jacobi, C., et al. (2024). Mesosphere and lower thermosphere wind perturbations due to the 2022 hunga tonga-hunga ha'apai eruption as observed by multistatic specular meteor radars. *Radio Sci.* 59, e2024RS008013. doi:10.1029/2024RS008013

Dong, W., Zhang, S., Huang, C., Huang, K., Gong, Y., and Gan, Q. (2018). A numerical study of gravity wave propagation characteristics in the stratospheric thermal duct. *J. Geophys. Res. Atmos.* 123, 11918–11937. doi:10.1029/2018JD029190

Dong, W., Fritts, D. C., Lund, T. S., Scott, A. W., and Zhang, S. (2020). Self-acceleration and instability of gravity wave packets: 2. Two-dimensional packet propagation, instability dynamics, and transient flow responses. *J. Geophys. Res. Atmos.* 125, e2019JD030691. doi:10.1029/2019JD030691

Dong, W., Fritts, D. C., Thomas, G. E., and Lund, T. S. (2021a). Modeling responses of polar mesospheric clouds to gravity wave and instability dynamics and induced large-scale motions. *J. Geophys. Res. Atmos.* 126, e2021JD034643. doi:10.1029/2021JD034643

Dong, W., Hickey, M. P., and Zhang, S. (2021b). A numerical study of gravity waves propagation characteristics in the mesospheric doppler duct. *J. Geophys. Res. Atmos.* 126, e2021JD034680. doi:10.1029/2021JD034680

Dong, W., Fritts, D. C., Hickey, M. P., Liu, A. Z., Lund, T. S., Zhang, S., et al. (2022). Modeling studies of gravity wave dynamics in highly structured environments: reflection, trapping, instability, momentum transport, secondary gravity waves, and induced flow responses. *J. Geophys. Res. Atmos.* 127, e2021JD035894. doi:10.1029/2021JD035894

Dong, W., Fritts, D. C., Liu, A. Z., Lund, T. S., and Hiu, H. (2023). Gravity waves emitted from kelvin-helmholtz instabilities. *Geophys. Res. Lett.* 50, e2022GL102674. doi:10.1029/2022GL102674

Ern, M., Preusse, P., Alexander, M. J., and Warner, C. D. (2004). Absolute values of gravity wave momentum flux derived from satellite data. *J. Geophys. Res. Atmos.* 109, D20103. doi:10.1029/2004JD004752

Franco-Diaz, E., Gerding, M., Holt, L., Strelnikova, I., Wing, R., Baumgarten, G., et al. (2024). Convective gravity wave events during summer near 54°n, present in both airs and rayleigh–mie–raman (Rmr) lidar observations. *Atmos. Chem. Phys.* 24, 1543–1558. doi:10.5194/acp-24-1543-2024

Fritts, D. C., and Alexander, M. J. (2003). Gravity wave dynamics and effects in the middle atmosphere. *Rev. Geophys.* 41, 1003. doi:10.1029/2001RG000106

Fritts, D. C., Dong, W., Lund, T. S., Brain, L., and Laughman, B. (2020). Self-acceleration and instability of gravity wave packets: 3. Three-dimensional packet propagation, secondary gravity waves, momentum transport, and transient mean forcing in tidal winds. *J. Geophys. Res. Atmos.* 125, e2019JD030692. doi:10.1029/2019JD030692

Gisinger, S., Polichtchouk, I., Dörnbrack, A., Reichert, R., Kaifler, B., Kaifler, N., et al. (2022). Gravity-wave-driven seasonal variability of temperature differences between ecmwf ifs and rayleigh lidar measurements in the lee of the southern andes. *J. Geophys. Res. Atmos.* 127, e2021JD036270. doi:10.1029/2021JD036270

Guo, Y., Liu, A. Z., Cai, X., and Swenson, G. R. (2020). Seasonal variation of vertical heat and energy fluxes due to dissipating gravity waves in the mesopause region over the andes. *J. Geophys. Res. Atmos.* 125, e2020JD033825. doi:10.1029/2020JD033825

Heale, C. J., Bossert, K., Vadas, S. L., Hoffmann, L., Dörnbrack, A., Stober, G., et al. (2020a). Secondary gravity waves generated by breaking mountain waves over Europe. *J. Geophys. Res. Atmos.* 125, e2019JD031662. doi:10.1029/2019JD031662

Heale, C. J., Lund, T. S., and Fritts, D. C. (2020b). Convectively generated gravity waves during solstice and equinox conditions. *J. Geophys. Res. Atmos.* 125, e2019JD031582. doi:10.1029/2019JD031582

Hersbach, H., Bell, B., Berrisford, P., Hirahara, S., Horányi, A., Muñoz-Sabater, J., et al. (2020). The era5 global reanalysis. *Q. J. R. Meteorological Soc.* 146, 1999–2049. doi:10.1002/qj.3803

Hindley, N. P., Wright, C. J., Hoffmann, L., Moffat-Griffin, T., and Mitchell, N. J. (2020). An 18-year climatology of directional stratospheric gravity wave momentum flux from 3-d satellite observations. *Geophys. Res. Lett.* 47, e2020GL089557. doi:10.1029/2020GL089557

Hoffmann, L., and Alexander, M. J. (2009). Retrieval of stratospheric temperatures from atmospheric infrared sounder radiance measurements. *J. Geophys. Res. Atmos.* 114, D07105. doi:10.1029/2008JD011241

Hoffmann, L., and Alexander, M. J. (2010). Occurrence frequency of convective gravity waves during the north american thunderstorm season. *J. Geophys. Res. Atmos.* 115, D20111. doi:10.1029/2010JD014401

Hoffmann, L., Xue, X., and Alexander, M. J. (2013). A global view of stratospheric gravity wave hotspots located with atmospheric infrared sounder observations. *J. Geophys. Res. Atmos.* 118, 416–434. doi:10.1029/2012JD018658

Hoffmann, L., Grimsdell, A. W., and Alexander, M. J. (2016). Stratospheric gravity waves at southern hemisphere orographic hotspots: 2003–2014 airs/aqua observations. *Atmos. Chem. Phys.* 16, 9381–9397. doi:10.5194/acp-16-9381-2016

Inchin, P. A., Guerrero, J. A., Snively, J. B., and Kaneko, Y. (2022). Simulation of infrasonic acoustic wave imprints on airglow layers during the 2016 m7.8 kaikoura earthquake. *J. Geophys. Res. Space Phys.* 127, e2021JA029529. doi:10.1029/2021JA029529

Kaifler, N., Kaifler, B., Dörnbrack, A., Rapp, M., Hormaechea, J. L., and de la Torre, A. (2020). Lidar observations of large-amplitude mountain waves in the stratosphere above tierra del fuego, argentina. *Sci. Rep.* 10, 14529. doi:10.1038/s41598-020-71443-7

Krasauskas, L., Kaifler, B., Rhode, S., Ungermann, J., Woiwode, W., and Preusse, P. (2023). Oblique propagation and refraction of gravity waves over the andes observed by gloria and alima during the southtrac campaign. *J. Geophys. Res. Atmos.* 128, e2022JD037798. doi:10.1029/2022JD037798

Liu, H.-L., McInerney, J. M., Santos, S., Lauritzen, P. H., Taylor, M. A., and Pedatella, N. M. (2014). Gravity waves simulated by high-resolution whole atmosphere community climate model. *Geophys. Res. Lett.* 41, 9106–9112. doi:10.1002/2014GL062468

Liu, A. Z., Guo, Y., Vargas, F., and Swenson, G. R. (2016). First measurement of horizontal wind and temperature in the lower thermosphere (105–140 km) with a na lidar at andes lidar observatory. *Geophys. Res. Lett.* 43, 2374–2380. doi:10.1002/2016GL068461

Lund, T. S., Fritts, D. C., Wan, K., Laughman, B., and Liu, H.-L. (2020). Numerical simulation of mountain waves over the southern andes. part i: mountain wave and secondary wave character, evolutions, and breaking. *J. Atmos. Sci.* 77, 4337–4356. doi:10.1175/jas-d-19-0356.1

Mandal, S., Moffat-Griffin, T., Wright, C. J., Pautet, P.-D., Taylor, M. J., and Nakamura, T. (2025). Gravity wave variability in the arctic winter mesosphere in relation with the stratospheric polar vortex. *J. Geophys. Res. Atmos.* 130, e2024JD043037. doi:10.1029/2024JD043037

Noble, P. E., Rhode, S., Hindley, N. P., Berthelemy, P., Moffat-Griffin, T., Preusse, P., et al. (2024). Exploring sources of gravity waves in the southern winter stratosphere using 3-d satellite observations and backward ray-tracing. *J. Geophys. Res. Atmos.* 129, e2024JD041294. doi:10.1029/2024JD041294

Sato, K., Watanabe, S., Kawatani, Y., Tomikawa, Y., Miyazaki, K., and Takahashi, M. (2009). On the origins of mesospheric gravity waves. *Geophys. Res. Lett.* 36, L19801. doi:10.1029/2009GL039908

Vadas, S. L., Zhao, J., Chu, X., and Becker, E. (2018). The excitation of secondary gravity waves from local body forces: theory and observation. *J. Geophys. Res. Atmos.* 123, 9296–9325. doi:10.1029/2017JD027970

Wing, R., Strelnikova, I., Dörnbrack, A., Gerding, M., Franco-Diaz, E., Holt, L., et al. (2025). Direct observation of quasi-monochromatic gravity wave packets associated with the polar night jet using a doppler-rayleigh lidar. *J. Geophys. Res. Atmos.* 130, e2025JD043707. doi:10.1029/2025JD043707

Wright, C. J., Hoffmann, L., Eckermann, S. D., Ern, M., and Alexander, M. J. (2017). Exploring gravity wave characteristics in 3-d using a novel s-transform technique: Airs/aqua measurements over the southern andes and drake passage. *Atmos. Chem. Phys.* 17, 8553–8575. doi:10.5194/acp-17-8553-2017

Yang, F., and Liu, A. Z. (2022). Stability characteristics of the mesopause region above the andes. *J. Geophys. Res. Space Phys.* 127, e2022JA030315. doi:10.1029/2022JA030315